PAPER

Check for updates

Electrocatalytic urea synthesis from NO and CO_2 on In_1Pd single atom alloys

Tingting Wu,*[a] Zihan Tian,[a] Ziyang Zhang,[a] Ye Tian [ID][a] and Ke Chu [ID]*[b]

Electrocatalytic urea synthesis from CO_2/NO co-electrolysis (EUCN) has emerged as a promising strategy for sustainable urea production, while simultaneously mitigating greenhouse gas emissions and NO pollutants. Herein, we have developed single-atom In_1 alloyed Pd (In_1Pd) as a high-performance EUCN catalyst, delivering a remarkable FE_{urea} of 45.9% and a urea yield rate of 55.2 mmol h^{-1} g^{-1} in a membrane electrode assembly electrolyzer. The combination of *in situ* spectroscopic measurements and theoretical calculations reveals the synergy of In_1 and Pd, which enables the co-activation of CO_2/NO and their C–N coupling while hampering the competing reactions, leading to greatly enhanced EUCN activity and selectivity.

Urea is a vital nitrogen fertilizer that is widely used in global agriculture.[1–3] Currently, the Bosch–Meiser process serves as the primary industrial route for urea synthesis, accounting for over 2% of global energy consumption and generating substantial CO_2 emissions.[4–8] Electrocatalytic urea synthesis from co-reduction of CO_2 and NO (EUCN) has emerged as a promising strategy for sustainable urea production, while simultaneously mitigating greenhouse gas emissions and NO pollutants.[9] However, the EUCN process involves a complex multistep reaction pathway requiring the activation of inert CO_2 and NO molecules and enhanced C–N coupling kinetics, posing significant challenges for catalyst design.[10] Current catalysts still suffer from low urea faradaic efficiency (FE_{urea}) and poor selectivity due possibly to the competitive side reactions (*i.e.*, the hydrogen evolution reaction (HER)) and independent reduction pathways.[9] Therefore, the development of high-performance catalysts with high activity, selectivity and durability is crucial to advance the practical application of EUCN.

Single-atom alloys (SAAs), which combine the merits of single-atom catalysts and alloy catalysts, have garnered significant attention in various electrocatalytic reactions involving both carbon and nitrogen cycles,[11–13] thus demonstrating their considerable potential for electrocatalytic urea synthesis from CO_2/NO co-electrolysis (EUCN). Among them, Pd-based materials have shown particular efficacy attributed to their unfilled d-electron orbitals ($4d^{10}$) that facilitate optimized adsorption/desorption behavior of key intermediates.[14–16] Nevertheless, Pd-based catalysts often suffer from insufficient

co-activation capability toward both nitrogen and carbon sources. Additionally, Pd exhibits a strong tendency for H adsorption,[17] which competes with the C–N coupling reaction and diminishes both EUCN activity and selectivity for urea synthesis. Notably, these limitations may be effectively mitigated by incorporating p-block metals such as indium (In). By virtue of its partially occupied p-orbitals, In can intrinsically hinder H binding,[18] while promoting CO_2 reduction to generate and stabilize C-intermediates beneficial for coupling with N-intermediates towards urea generation.[19–21] Motivated by these insights, we propose that single-atom In alloyed with Pd (In_1Pd) may serve as a highly promising catalyst, enabling enhanced activity and selectivity for efficient EUCN.

In this study, we developed In_1Pd as a highly active and selective EUCN catalyst for urea electrosynthesis. Notably, the In_1Pd catalyst exhibits exceptional performance in a membrane electrode assembly (MEA) electrolyzer, delivering a remarkable FE_{urea} of 45.9% and a urea yield rate of 55.2 mmol h^{-1} g^{-1} at −0.7 V. The catalytic EUCN mechanism of the In_1Pd catalyst is further elucidated through combined *in situ* spectroscopic measurements and theoretical calculations, revealing that the enhanced EUCN efficiency of In_1Pd stems from the synergistic effect of In_1 and Pd, which promotes the co-activation of CO_2 and NO to *CO/*NH_2 and their C–N coupling.

In_1Pd was synthesized *via* a one-pot wet chemistry method. The XRD patterns (Fig. 1a) reveal that In_1Pd retains the crystalline structure of pristine Pd (JCPDS No. 65-2867), suggesting that In_1 incorporation does not change the crystalline phase of pristine Pd. The TEM image (Fig. 1b) shows that In_1Pd exhibits a typical graphene-like morphology. Elemental mapping images of In_1Pd (Fig. 1c) illustrate a uniform distribution of In_1 atoms on Pd. The coordination structure and electronic characteristics of In_1Pd are systematically characterized *via*

[a] College of Science, Hebei North University, Zhangjiakou 075000, Hebei, China. E-mail: 1329271270@qq.com

[b] School of Materials Science and Engineering, Lanzhou Jiaotong University, Lanzhou 730070, China. E-mail: chuk630@mail.lzjtu.cn
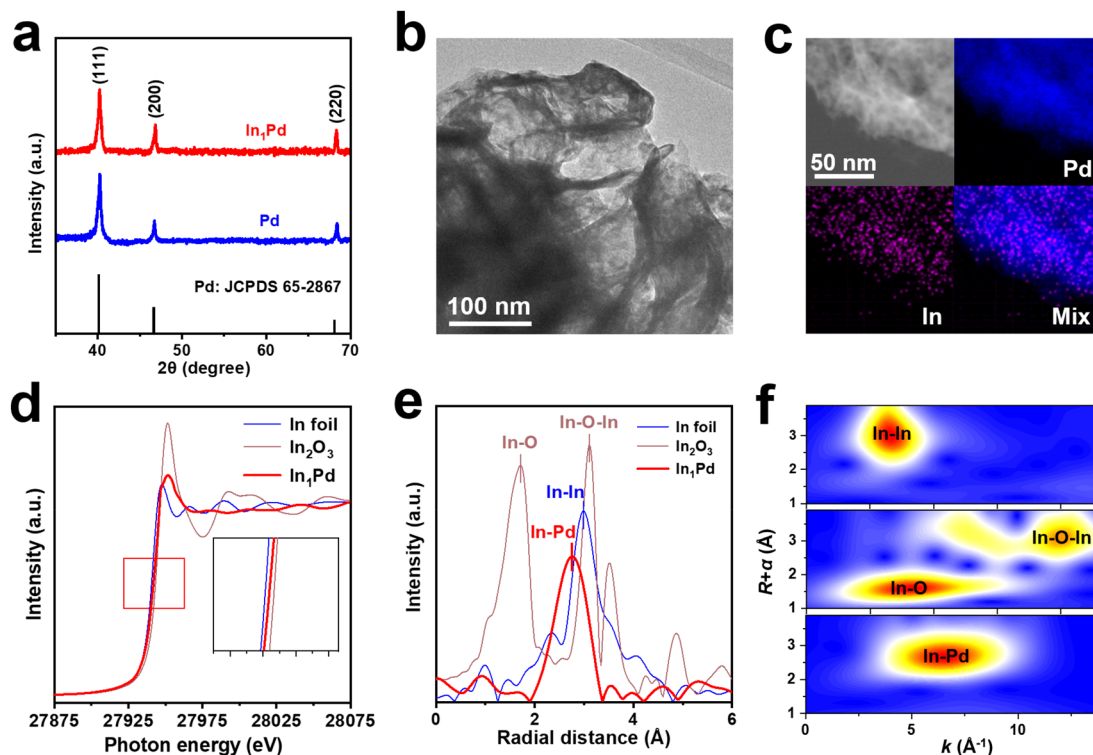
Fig. 1 Characterization of In_1Pd: (a) XRD patterns, (b) TEM image, (c) elemental mapping images, (d) In K-edge XANES, (e) EXAFS spectra and (f) WT analyses of In_1Pd and reference samples.

X-ray absorption spectroscopy. The XANES analysis at the In K-edge (Fig. 1d) reveals that the absorption edge of In_1Pd lies between In foil and In_2O_3 reference samples, indicating an In oxidation state between 0 and +3, which arises from electron transfer from In_1 to Pd due to the lower electronegativity of In (1.78) relative to Pd (2.20). The EXAFS spectra (Fig. 1e) show that In_1Pd exhibits a prominent In–Pd coordination peak at 2.75 Å, with no observable In–In or In–Pd coordination bonds, confirming the atomic dispersion of In on the Pd substrate.[22–24] The corresponding wavelet transform (WT) analysis (Fig. 1f) displays a single In–Pd coordination peak at 6.5 Å^{-1}, further verifying the monoatomic In dispersion within the Pd matrix.

The electronic structure of In_1Pd is systematically investigated using DFT calculations. Electron density difference analysis (Fig. S1a) reveals a distinct electron transfer from In_1 to Pd, in line with the XANES result (Fig. 1d). This interfacial In_1–Pd electron interaction guarantees the robust bonding between In_1 and the Pd substrate, which endows In_1Pd with exceptional structural stability. The corresponding PDOS analysis (Fig. S1b) presents favorable orbital overlapping between the 5p orbital of In_1 and the 4d orbital of Pd, offering a theoretical foundation for the efficient charge transfer and robust structural stability.[25] Additionally, *ab initio* molecular dynamics (AIMD) simulation results (Fig. S2) indicate that In_1Pd maintains stable energy and temperature profiles

throughout the simulation, further validating its excellent thermal stability.[26–30]

The EUCN performance of In_1Pd is assessed in a MEA cell containing 0.1 M $KHCO_3$ catholyte saturated with humidified NO and CO_2. Gas and liquid products are quantified by gas chromatography and colorimetry, respectively (Fig. S3). LSV curves (Fig. 2a) show a relatively low current density of In_1Pd in sole CO_2-saturated electrolyte. Strikingly, the current density is significantly enhanced in the presence of both NO and CO_2, suggesting the high catalytic EUCN activity of In_1Pd toward urea synthesis. The EUCN performance of In_1Pd is quantitatively evaluated after 1 h of electrolysis. Remarkably, In_1Pd achieves the highest FE_{urea} of 45.9% at −0.7 V, with a corresponding urea yield rate of 55.2 mmol h^{-1} g^{-1} (Fig. 2b), surpassing most recently reported catalysts for urea electrosynthesis (Fig. S4 and Table S1). Control experiments are conducted to validate the nitrogen and carbon sources (Fig. S5). No urea formation is observed under conditions lacking NO or CO_2, or at the open-circuit potential (OCP), effectively ruling out the possibility of system contamination as C/N sources of urea. Further ^{13}C and ^{15}N isotope tracing *via* nuclear magnetic resonance (NMR) spectroscopy, using $^{13}CO_2$ (Fig. 2c) and ^{15}NO (Fig. 2d) as tracers, reveals the characteristic signals of $^{13}CO(NH_2)_2$ and $CO(^{15}NH_2)_2$, respectively, further confirming that the synthesized urea originates exclusively from the EUNC process catalyzed by In_1Pd.
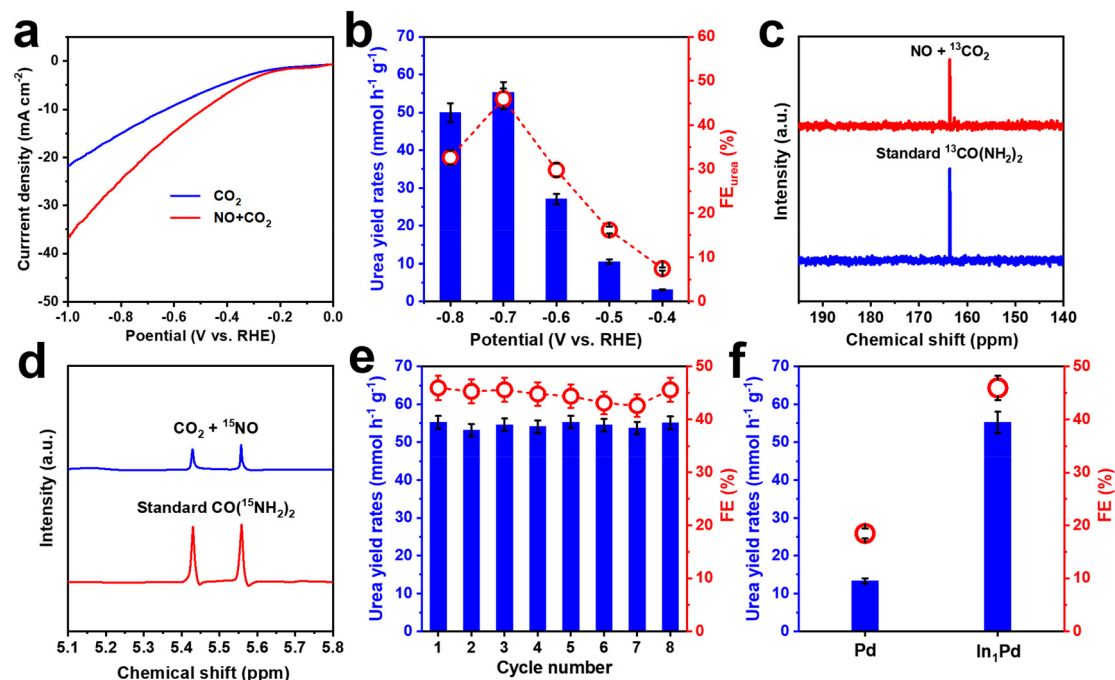
Fig. 2 (a) LSV curves of In_1Pd under different conditions. (b) Urea yield rates and FE_{urea} of In_1Pd at various potentials. (c) ^{13}C NMR spectra of the $^{13}CO(NH_2)_2$ standard sample and those fed by $^{13}CO_2$ after electrolysis at −0.7 V. (d) ^1H NMR spectra of the $CO(^{15}NH_2)_2$ standard sample and those electrolyzed in ^{15}NO electrolyte at −0.7 V. (e) Urea yield rates and FE_{urea} during eight cycling tests at −0.7 V. (f) Comparison of urea yield rates and FE_{urea} between pristine Pd and In_1Pd at −0.7 V.

The selectivity of In_1Pd toward ECNU is evaluated by quantifying the FEs of other byproducts (CO, H_2 and NH_4^+). At the optimal applied potential of −0.7 V, FE_{urea} remains significantly higher than the FEs of all byproducts (Fig. S6), confirming the exceptional ECNU selectivity of In_1Pd for urea synthesis. For stability evaluation, we conducted an eight-cycle test, which shows that both urea yield rate and FE_{urea} exhibit minimal fluctuations (Fig. 2e), confirming the excellent catalysis durability of In_1Pd.[30–32] Comparative analysis shows that the pristine Pd catalyst (Fig. 2f) exhibits a much inferior ECNU performance relative to In_1Pd, highlighting the critical synergistic interaction between In_1 and the Pd substrate in boosting the ECNU activity.

To elucidate the fundamental understanding of the significantly improved EUCN performance of In_1Pd, we employed *in situ* FTIR and online differential electrochemical mass spectrometry (DEMS) to identify the reaction intermediates. First, *in situ* FTIR measurements are conducted on In_1Pd over the potential range from the OCP to −0.7 V. As shown in Fig. 3a–c, the characteristic peak at 1396 cm^{-1} is assigned to the symmetric stretching vibration of the *COOH intermediate, while the C=O stretching peak at 2017 cm^{-1} corresponds to the generated *CO intermediate[33] (Fig. 3b). Notably, additional peaks observed at 1695 cm^{-1} and 1433 cm^{-1} are attributed to *CONH_2 intermediates and C–N bonds,[34–36] respectively (Fig. 3c), indicating that EUCN proceeds *via* *NH_2 + *CO → *NH_2CO. Meanwhile, the enhanced peak intensity of urea (1610/1195 cm^{-1}) with increasing potentials indicates that the

generated *NH_2CO intermediates are readily converted into urea.[35] In addition, online DEMS measurements (Fig. 3d) show the prominent *m/z* signals corresponding to key intermediates and products, including *$CONH_2$ (*m/z* = 44), *$CO(NH_2)_2$ (*m/z* = 60), *NO (*m/z* = 30), *NH_2 (*m/z* = 16), *CO (*m/z* = 28) and *COOH (*m/z* = 45). These DEMS results are in line with *in situ* FTIR data, collectively providing compelling evidence that In_1Pd facilitates the efficient co-reduction of CO_2 and NO to urea through a sequential relay catalysis mechanism (Fig. S7), where In_1Pd first promotes the co-activation of CO_2 and NO, forming critical *CO and *NH_2 intermediates. These *CO/*NH_2 intermediates then undergo C–N coupling to generate *$CONH_2$, which is ultimately converted into urea.

DFT calculations are utilized to unravel the atomic-level EUCN mechanism of In_1Pd. Given that the adsorption and activation of NO/CO_2 represent the initial step of the catalytic EUCN process, our analysis first focused on NO/CO_2 adsorption behaviors on both In_1 and Pd sites of In_1Pd. As illustrated in Fig. S8, the adsorption free energy calculations reveal that In_1 sites are more favorable for CO_2 adsorption (−0.26 eV), while Pd sites are more favorable for NO adsorption (−0.48 eV), suggesting that during the EUCN process, In_1 sites primarily facilitate CO_2 reduction while Pd sites dominate NO reduction.

We then constructed the free energy diagram for the conversion of CO_2 to *CO on In_1 sites (Fig. 4a), with the corresponding intermediate configurations shown in Fig. S9. Calculation results reveal that the rate-determining step (RDS)
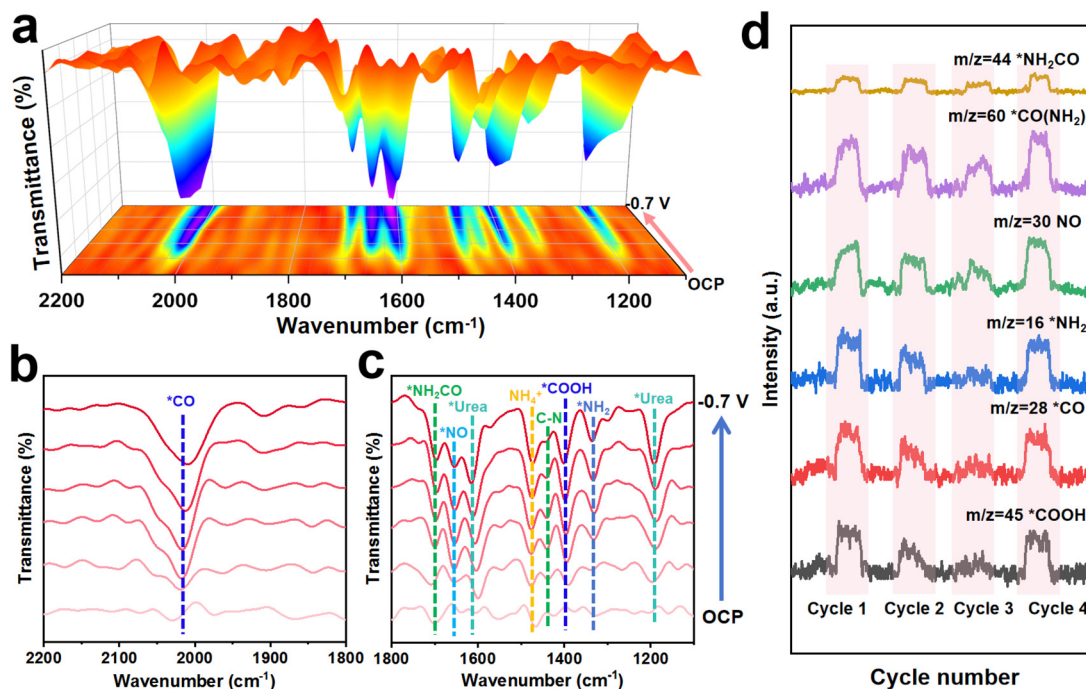
Fig. 3 (a–c) *In situ* FTIR spectra of In$_1$Pd during the EUNC electrolysis at different potentials from the OCP to −0.7 V. (d) Online DEMS spectra of In$_1$Pd at −0.7 V.
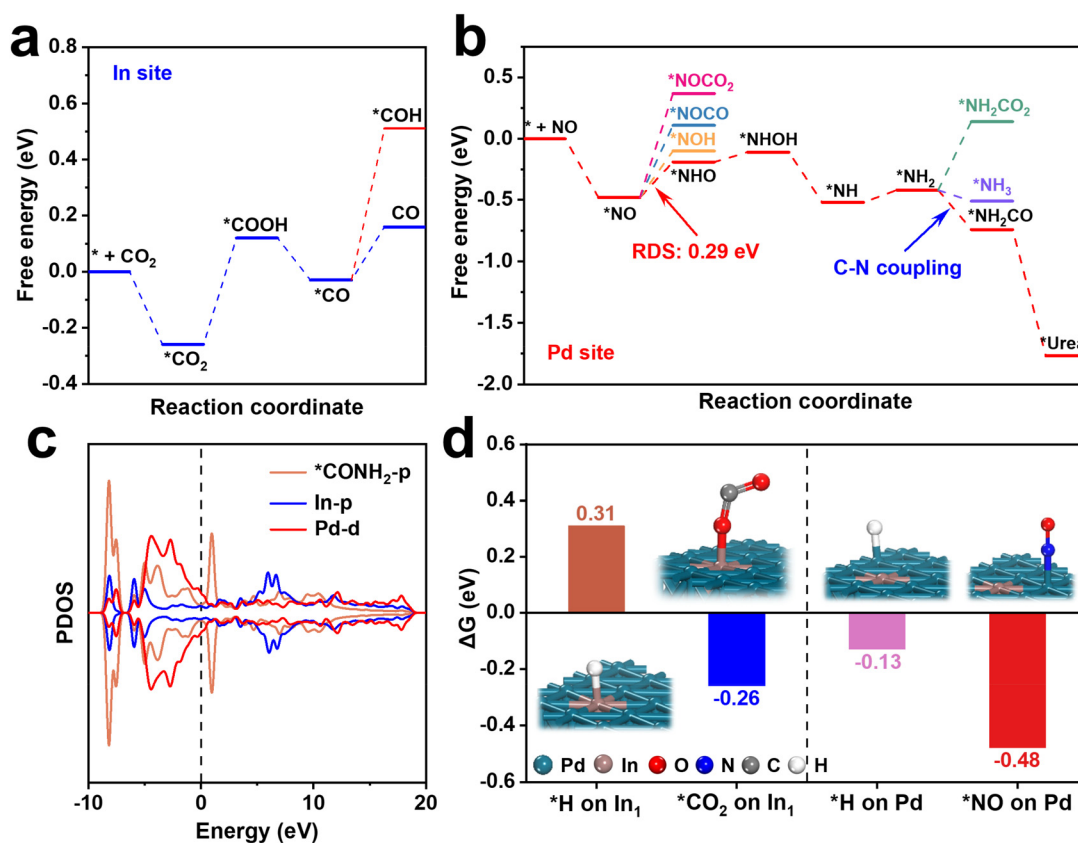

Fig. 4 (a) Free energy diagram of the CO$_2$ → CO pathway on In$_1$ sites. (b) Free energy diagram of the entire EUNC pathway on Pd sites and possible competing side reactions. (c) PDOS profile of *CONH$_2$ on In$_1$Pd. (d) Adsorption free energies of *H/*CO$_2$ on In$_1$ sites and *H/*NO on Pd sites.

for $CO_2 \to *CO$ reduction is the first CO_2 hydrogenation ($*CO_2$ + $*H \to *COOH$), with an energy barrier of 0.38 eV. Notably, the $*CO$ desorption energy barrier on In_1 sites is significantly lower (0.19 eV) than that required for further hydrogenation ($*CO + *H \to *COH$, 0.54 eV), indicating that $*CO$ generated on In_1 sites is more inclined to desorb and spontaneously migrate closer to Pd sites and participate in the C–N coupling reaction.

Subsequently, we constructed the free energy diagram for the entire EUCN process on Pd sites, with the corresponding intermediate configurations shown in Fig. S10. As illustrated in Fig. 4b, the RDS of this pathway is also the initial NO hydrogenation ($*NO + *H \to *NHO$, 0.29 eV). Further analysis of the energy barriers for the competing reactions, such as $*NO + *CO \to *NOCO$ and $*NO + *CO_2 \to *NOCO_2$, reveals that compared to direct C–N coupling with $*CO$ or $*CO_2$, $*NO$ tends to undergo hydrogenation reduction *via* the NHO pathway. Significantly, after stepwise $*NOH$ reduction to $*NH_2$, the generated $*NH_2$ intermediate is more likely to undergo C–N coupling with $*CO$ to form $*NH_2CO$ relative to other competing reactions ($*NH_2 + H \to *NH_3$, $*NH_2 + CO_2 \to *NH_2CO_2$). The generated $*NH_2CO$ can be spontaneously converted into urea. These findings correlate closely with the above *in situ* FTIR and DEMS results (Fig. 3).

For the critical $*NH_2CO$ intermediate on both pristine Pd and In_1Pd surfaces (Fig. S11), the charge density difference map displays that In_1Pd provides more electrons to $*NH_2CO$ than pristine Pd does, suggesting the significantly enhanced $*NH_2CO$ stabilization on In_1Pd. Further PDOS analysis (Fig. 4c and Fig. S12) reveals that compared to pristine Pd, the overlap region of electron orbitals between In_1Pd and $*NH_2CO$ is much expanded, further verifying the stronger $*NH_2CO$ activation capability of In_1Pd. These results indicate that the introduced In_1 not only promotes the reduction of CO_2 to $*CO$ but also modulates the electronic structure of the Pd substrate and enhances $*NH_2CO$ stabilization and activation towards urea conversion. Given the HER as the major competing reaction for the EUCN,[4] we examined the adsorption characteristics of $*H$ on In_1Pd. Fig. 4d shows that In_1 sites are more favorable for adsorbing $*CO_2$ over $*H$, while Pd sites exhibit a stronger tendency to adsorb $*NO$ over $*H$. Molecular dynamics (MD) simulations (Fig. S13) further reveal a more pronounced enrichment effect of $*NO$ on the In_1Pd surface, and the corresponding radial distribution function (RDF, Fig. S14) shows that the NO/In_1Pd interaction is stronger than the H/In_1Pd interaction. These results demonstrate that In_1Pd can well hamper the competing HER towards the selective conversion of CO_2/NO to urea.

In summary, In_1Pd is demonstrated as a high-performance EUCN catalyst for urea electrosynthesis. Combined *in situ* spectroscopic measurements and theoretical calculations reveal that the enhanced EUCN performance of In_1Pd stems from the synergy of In_1 and Pd, which enables the co-activation of CO_2/NO and their C–N coupling, while hampering the competing reactions. Impressively, In_1Pd exhibits an unprecedented urea synthesis performance with urea yield rate up to 55.2 mmol h^{-1} g^{-1} and FE$_{urea}$ of 45.9% in a MEA cell. This work provides in-depth insights into the EUCN mechanism and opens up a new avenue for developing efficient and robust catalysts.

Conflicts of interest

There are no conflicts of interest to declare.

Data availability

The data supporting this article have been included as part of the SI. Supplementary information is available. See DOI: https://doi.org/10.1039/d5dt02018b.

Acknowledgements

References

1 Y. Kohlhaas, Y. S. Tschauder, W. Plischka, U. Simon, R.-A. Eichel, M. Wessling and R. Keller, *Joule*, 2024, **8**, 1579–1600.
2 C. Mao, J. Byun, H. W. MacLeod, C. T. Maravelias and G. A. Ozin, *Joule*, 2024, **8**, 1224–1238.
3 R. Ge, J. Huo, P. Lu, Y. Dou, Z. Bai, W. Li, H. Liu, B. Fei and S. Dou, *Adv. Mater.*, 2024, **36**, 2412031.
4 X. Peng, L. Zeng, D. Wang, Z. Liu, Y. Li, Z. Li, B. Yang, L. Lei, L. Dai and Y. Hou, *Chem. Soc. Rev.*, 2023, **52**, 2193–2237.
5 J. Liu, S. Zhang, Y. Jiang, W. Li, M. Jin, J. Ding, Y. Zhang, G. Wang and H. Zhang, *Chem. Commun.*, 2024, **60**, 11592–11595.
6 Y. Wu, H. Lin, Q. Mao, H. Yu, K. Deng, J. Wang, L. Wang, Z. Wang and H. Wang, *Small*, 2024, **20**, 2407679.
7 S. Zhang, M. Jin, H. Xu, X. Zhang, T. Shi, Y. Ye, Y. Lin, L. Zheng, G. Wang, Y. Zhang, H. Yin, H. Zhang and H. Zhao, *Energy Environ. Sci.*, 2024, **17**, 1950–1960.
8 Z. Wang, Y. Wang, S. Xu, K. Deng, H. Yu, Y. Xu, H. Wang and L. Wang, *J. Mater. Chem. A*, 2025, **13**, 305–311.
9 Y. Huang, R. Yang, C. Wang, N. Meng, Y. Shi, Y. Yu and B. Zhang, *ACS Energy Lett.*, 2022, **7**, 284–291.
10 D. Chen, J. Liu, J. Shen, Y. Zhang, H. Shao, C. Chen and S. Wang, *Adv. Energy Mater.*, 2024, **14**, 2303820.
11 R. T. Hannagan, G. Giannakakis, M. Flytzani-Stephanopoulos and E. C. H. Sykes, *Chem. Rev.*, 2020, **120**, 12044–12088.
12 T. Zhang, A. G. Walsh, J. Yu and P. Zhang, *Chem. Soc. Rev.*, 2021, **50**, 569–588.
13 M. Xu, F. Wu, Y. Zhang, Y. Yao, G. Zhu, X. Li, L. Chen, G. Jia, X. Wu, Y. Huang, P. Gao and W. Ye, *Nat. Commun.*, 2023, **14**, 6994.

14 S. Zhang, J. Geng, Z. Zhao, M. Jin, W. Li, Y. Ye, K. Li, G. Wang, Y. Zhang, H. Yin, H. Zhang and H. Zhao, *EES Catal.*, 2023, **1**, 45–53.

15 K. Chen, D. Ma, Y. Zhang, F. Wang, X. Yang, X. Wang, H. Zhang, X. Liu, R. Bao and K. Chu, *Adv. Mater.*, 2024, **36**, 2402160.

16 K. Chen, J. Xiang, Y. Guo, X. Liu, X. Li and K. Chu, *Nano Lett.*, 2024, **24**, 541–548.

17 X. Li, P. Shen, X. Li, D. Ma and K. Chu, *ACS Nano*, 2023, **17**, 1081–1090.

18 P. Lu, X. Tan, H. Zhao, Q. Xiang, K. Liu, X. Zhao, X. Yin, X. Li, X. Hai and S. Xi, *ACS Nano*, 2021, **15**, 5671–5678.

19 W. Guo, X. Tan, J. Bi, L. Xu, D. Yang, C. Chen, Q. Zhu, J. Ma, A. Tayal and J. Ma, *J. Am. Chem. Soc.*, 2021, **143**, 6877–6885.

20 J. Li, M. Zhu and Y. F. Han, *ChemCatChem*, 2021, **13**, 514–531.

21 S. Li, X. Lu, S. Zhao, M. Ceccato, X.-M. Hu, A. Roldan, M. Liu and K. Daasbjerg, *ACS Catal.*, 2022, **12**, 7386–7395.

22 R. Lang, X. Du, Y. Huang, X. Jiang, Q. Zhang, Y. Guo, K. Liu, B. Qiao, A. Wang and T. Zhang, *Chem. Rev.*, 2020, **120**, 11986–12043.

23 S. K. Kaiser, Z. Chen, D. Faust Akl, S. Mitchell and J. Pérez-Ramírez, *Chem. Rev.*, 2020, **120**, 11703–11809.

24 C. Gao, J. Low, R. Long, T. Kong, J. Zhu and Y. Xiong, *Chem. Rev.*, 2020, **120**, 12175–12216.

25 D. Wu, K. Chen, P. Lv, Z. Ma, K. Chu and D. Ma, *Nano Lett.*, 2024, **24**, 8502–8509.

26 J. Min, J. Zhai, T. Dong, D. Xu, Y. Yan, C. S. Garoufalis, S. Baskoutas, Z. Zeng and Y. Jia, *Nano Lett.*, 2023, **23**, 4648–4653.

27 J. Zhai, T. Dong, Y. Zhou, J. Min, Y. Yan, C. S. Garoufalis, S. Baskoutas, D. Xu and Z. Zeng, *Nano Lett.*, 2023, **23**, 3239–3244.

28 Z. Zhao, J. Zhang, M. Lei and Y. Lum, *Nano Res. Energy*, 2023, **2**, e9120044.

29 W. Gou, H. Sun and F. Cheng, *Nano Res. Energy*, 2024, **3**, e9120121.

30 Q. Wang, H. Wei, P. Liu, Z. Su and X.-Q. Gong, *Nano Res. Energy*, 2024, **3**, e9120112.

31 Y. Cheng, H. Wang, H. Song, K. Zhang, G. I. Waterhouse, J. Chang, Z. Tang and S. Lu, *Nano Res. Energy*, 2023, **2**, e9120082.

32 J. Shen and D. Wang, *Nano Res. Energy*, 2023, **3**, e9120096.

33 Q. Hu, W. Zhou, S. Qi, Q. Huo, X. Li, M. Lv, X. Chen, C. Feng, J. Yu, X. Chai, H. Yang and C. He, *Nat. Sustain.*, 2024, **7**, 442–451.

34 Y. Gao, J. Wang, M. Sun, Y. Jing, L. Chen, Z. Liang, Y. Yang, C. Zhang, J. Yao and X. Wang, *Angew. Chem., Int. Ed.*, 2024, **136**, e202402215.

35 Y. Luo, K. Xie, P. Ou, C. Lavallais, T. Peng, Z. Chen, Z. Zhang, N. Wang, X.-Y. Li, I. Grigioni, B. Liu, D. Sinton, J. B. Dunn and E. H. Sargent, *Nat. Catal.*, 2023, **6**, 939–948.

36 C. Lv, L. Zhong, H. Liu, Z. Fang, C. Yan, M. Chen, Y. Kong, C. Lee, D. Liu, S. Li, J. Liu, L. Song, G. Chen, Q. Yan and G. Yu, *Nat. Sustain.*, 2021, **4**, 868–876.